# Exploratory coupled channels calculations for loosely bound carbon isotopes

D. Ridikas, M.H. Smedberg, J.S. Vaagen, M.V. Zhukov

# GANIL

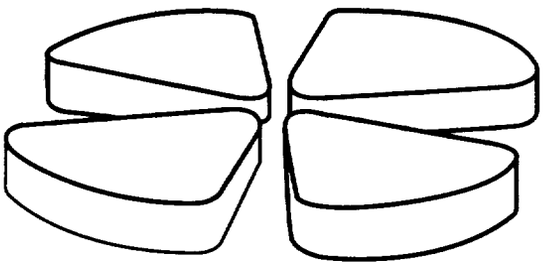



# Exploratory coupled channels calculations for loosely bound carbon isotopes

D. Ridikas[a,c], M.H. Smedberg[b], J.S. Vaagen[c,d] and M.V. Zhukov[b,d]

[a]GANIL (CEA/DSM-CNRS/IN2P3), BP 5027, F-14076 Caen Cedex 5, France



[b]Department of Physics, Chalmers University of Technology and Göteborg University, S-412 96 Göteborg, Sweden

[c]Department of Physics, University of Bergen, N-5007 Bergen, Norway

[d]NORDITA, Blegdamsvej 17, DK-2100 Copenhagen, Denmark

**GANIL P 97 20**

## 1. Introduction

Recently experimental evidence for a new one-neutron halo candidate, namely $^{19}$C, has become available. This has sparked off considerable interest as the only established one-neutron halo nucleus so far has been $^{11}$Be. The $^{11}$Be nucleus where relative $s$-motion dominates the ground state, has been extensively studied during the last few years [1–4] and has provided a testing ground for single-neutron halo theories. The measured longitudinal momentum distributions of $^{18}$C fragments [5] and neutrons from $^{19}$C breakup reactions [6] were reported to be very narrow compared with fragmentation of the neighbouring nucleus $^{18}$C. The one-neutron separation energy $S_n(^{19}\mathrm{C})$=242±95 keV [5] is an order of magnitude smaller than that of the core, $S_n(^{18}\mathrm{C})$=4180±30 keV [7], arguing for a binary model. Regrettably, $S_n(^{19}\mathrm{C})$ is determined with a precision which is far from satisfactory, but it appears to be even smaller than $S_n(^{11}\mathrm{Be})$=503±6 keV [8], suggesting that the halo of $^{19}$C could be even more pronounced if an $s$-wave halo neutron is involved.

The spin of the $^{19}$C ground state is not known experimentally yet [7], but three closely spaced low-lying states $1/2^+$, $3/2^+$, $5/2^+$ could be expected. In the naive independent particle model, the last neutron in $^{19}$C should be in $0d_{5/2}$ orbit; the $l$=2 centrifugal barrier would however strongly limit the extension of this halo [9], hence implying wide corresponding momentum distributions. More extensive shell model calculations based on the Warburton-Brown effective interaction [10] do, however, actually predict $s$-orbit dominance for the $^{19}$C ground state. The situation is very similar to the case of $^{11}$Be for which the same effective interaction correctly predicts $s$-wave dominance for the $J^\pi=1/2^+$ ground state. A recent relativistic mean field calculation [11] also predicts $J^\pi=1/2^+$. Such calculations are more reliable what concerns the trend in the binding with neutron number than concerning the actual separation energy for loosely bound systems.

The separation of core and halo properties is an approximation. It has become clear that inclusion of core excitations may improve aspects of the theoretical description of one-neutron halo systems. The halo neutron admixes components with the core in its ground state and in low-lying excited states, and this effect has proved to be very important for the description of $^{11}$Be (see [4] and references therein). Encouraged by the results of calculations for $^{11}$Be [1–4], we have applied the same *particle+core* cluster model to

$^{19}$C [12], although the experimental situation is less clear here than for $^{11}$Be. In this article we expand the discussion, including also a comparison with $^{17}$C. We compute overlap functions, the longitudinal momentum distribution for the core, the core-neutron distance and the *r.m.s.* matter radius, the $E1$ strength function and the neutron-stripping and electromagnetic dissociation (EMD) cross sections.

As an additional test, we also calculate the ground state of $^{17}$C, since data on measured longitudinal momentum distributions after fragmentation have become available [5,13]. The separation energy of the last neutron in this nucleus is again small, only $S_n(^{17}\mathrm{C})$=729±18 keV [14], and suggesting this to be another candidate for a one-neutron halo system. On the other hand, both shell model [10] and relativistic mean field calculations [11] argue for a $J^\pi$=3/2$^+$ non-halo ground state structure for this case.

In the following sections our results will be compared with available data and previous theoretical calculations for the loosely bound nuclei $^{17}$C and $^{19}$C. More information on these carbon isotopes will allow us to further explore the possible presence and characteristics of the halo phenomenon and to test the concepts developed for $^{11}$Be.

## 2. The Coupled Channels Formalism

Our model entails a coupled channels (CC) treatment involving a nonspherical nucleus, where the deformation of the potential implies a coupling between the collective degrees of freedom of a core and the orbital motion of a single neutron. The relationship between given states $|A\rangle$ and $|B\rangle$ of nuclei A and B=A+1 is expressed by the radial overlap functions $r\mathcal{R}^B_{ljA}(r)$ of the relative distance between the core and the neutron. For bound states these fall off exponentially, $exp(-\kappa^B_A r)$, for large $r$, with slopes $\kappa^B_A = \sqrt{2\mu E^B_A}/\hbar$ governed by the separation energy $E^B_A$=$S_n$(B)+E$^*_A$. Here $\mu$ stands for the reduced mass of the neutron with respect to the core, while $S_n$(B) is the one-neutron ground state separation energy of the nucleus B and $E^*_A$ is the excitation energy for the state $|A\rangle$ of the core nucleus. We have shown in [4] that the inclusion of core excited states will not affect the slope of the tail, but influences only its magnitude and the radial behaviour closer to the core.

The Hamiltonian describing the *particle+core* system is written in the form:

$$H = H_{core} + T + V\,, \tag{1}$$

where $T$ is the kinetic energy of the particle, and $V$ the deformed potential. The core energy is represented by $H_{core}$. Expansion of the total wave function (WF) solution to the Hamiltonian (1) into radial and angular parts in the space fixed frame,

$$\Psi_{JM} = \sum_{ljJ_c} \mathcal{R}^J_{ljJ_c}(r)\Phi_{ljJ_cJM}, \tag{2}$$

leads to non-adiabatic coupled radial channels equations [15] for the relative motion of the single nucleon with respect to the core:

$$\left\{-\frac{\hbar^2}{2\mu}\frac{d^2}{dr^2} + \frac{\hbar^2}{2\mu}\frac{l(l+1)}{r^2} + E^B_A\right\} r\mathcal{R}^J_{ljJ_c}(r) = -\sum_{l'j'J'_c} \langle l'j'J'_cJ|V|ljJ_cJ\rangle r\mathcal{R}^J_{l'j'J'_c}(r). \tag{3}$$

The channels are specified by the orbital and total angular momenta ($l$ and $j$) of a single nucleon, the angular momentum $J_c$ of the core, and the total angular momentum $J = j + J_c$ of the system. Note that CC equations like (3) hold for the radial overlap functions in general, without any rotor core assumption. For example, with a vibrational coupling model for $^{11}$Be [3] the results were similar to the ones obtained in the rotational coupling approach used in [1,2]. It is obvious, however, that in solving the CC equations a truncation should be performed, i.e. the coupling connects only a limited number of core states. In this exploratory calculation we include only two core states, namely the $0^+$ ground state and the first excited $2^+_1$ state.

The neutron-core model interaction is chosen to be a deformed Woods-Saxon potential (in the core rest frame)

$$V(R_0, a; r, \hat{r}) = \frac{V_{ws}}{1 + exp(\frac{r - R(R_0,\hat{r})}{a})}; \quad R(R_0, \hat{r}) = \frac{R_0}{\nu}\left(1 + \beta Y_{20}(\hat{r})\right). \tag{4}$$

Here $V_{ws}$ is the potential depth, $a$ the core diffuseness, and $\beta$ the deformation parameter for the core. The integral $\nu^3 = \int \frac{d\hat{r}}{4\pi}(1 + \beta Y_{20}(\hat{r}))^3$ in the denominator of Eq. (4) is included in order to preserve the volume for different choices of the deformation. For the WF, Eq. (2), the potential depth is fixed and depends on the total angular momentum $J$, the deformation parameter and the one-neutron separation energy. The spin-orbit

potential $V_{so}(r)$ is derived from the monopole part $V^0(r)$ of $V(R_0, a; r, \hat{r})$ in a standard way

$$V_{so}(r) = -2V_{so}(\frac{\hbar}{m_\pi c})^2(l \cdot s)\frac{1}{r}\frac{d}{dr}V^0(r) \tag{5}$$

For the spin-orbit strength $V_{so}$ we use the standard expression given by [15]

$$2V_{so}(\frac{\hbar}{m_\pi c})^2 = (22 - 14\frac{N-Z}{A})\, r_0^2; \quad r_0 \approx 1.2\ fm. \tag{6}$$

The deformation parameter can be estimated from the experimental $B(E2)$ transition strength if the relation

$$B(E2; 0^+_{gs} \rightarrow 2^+_1) = \left(\frac{3}{4\pi} Z R_0^2\right)^2 \beta^2. \tag{7}$$

is applied. Here we assume that the mass deformation for the core is the same as the charge deformation for the core.

To solve the system of CC equations we use the technique described in [16], expanding the radial wave functions in terms of complete sets of Sturmian functions $\{r\mathcal{R}^J_{ljJ_c}(r)\} = \sum_n C^i_{nlj}\mathcal{S}^i_{nlj}(r)$. All the basis functions in sets of $\{i = A \rightarrow B\}$ have the same asymptotic behaviour, determined by the energy $E^B_A$ treated as an input parameter. Thus, our expansion always reproduces the correct asymptotic slope. The algebraic eigenvalue problem is easily obtained by inserting $\sum_n C^i_{nlj}\mathcal{S}^i_{nlj}(r)$ into (3) and the resulting matrix equations are solved with standard diagonalization routines for symmetric matrices with respect to expansion coefficients and potential depths (see [16] for a more detailed discussion).

## 3. Longitudinal Momentum Distributions

A signature of a halo state is the narrow momentum distributions of the fragments (core and neutron) following breakup of a high energy beam of the nuclei of interest. This is a consequence of the Heisenberg uncertainty principle where an extended spatial distribution for the valence neutron implies a narrow distribution in momentum space. A measurement has been performed for the $^{18}$C ($^{16}$C) fragments from the breakup of $^{19}$C ($^{17}$C) on a beryllium target at 77 MeV/u (83 MeV/u), and the longitudinal momentum distributions were actually found to be narrow [5,13]. Also the observed narrow momentum distribution for neutrons in core breakup reactions at 30 MeV/u [6] supports the idea of an extended neutron halo in $^{19}$C.

At high energies and on light targets the observed core fragment momentum distribution has been identified with the ground state momentum distributions inside the nucleus. This identification, where the reaction mechanism is assumed to be very simple and not to add modifying terms, is referred to as the transparent limit of the Serber model [17] and just corresponds to the momentum distributions calculated from the Fourier transform of the radial WF. An improvement of this approximation can easily be made by taking absorption into account. For a single particle WF describing the relative motion between a valence neutron and the core,

$$\psi_{ljm}(r) = R_{lj}(r) \sum_{m_l,m_s} \langle lm_l \frac{1}{2} m_s | jm \rangle Y_{lm_l}(\hat{r}) \chi_{m_s}, \tag{8}$$

the momentum distribution of the core fragment in the projectile rest frame in a neutron stripping reaction is [18]

$$\frac{d\sigma_{-n}}{dk} = \frac{1}{(2\pi)^3} \frac{1}{2j+1} \sum_{m,m_s} \int db_n [1 - |S_n(b_n)|^2] \left| \langle exp(-ik \cdot r) \chi_{m_s} | S_c(b_c) | \psi_{ljm}(r) \rangle \right|^2, \tag{9}$$

where $b_n$ ($b_c$) is the two-dimensional impact parameter perpendicular to the beam axis of the valence neutron (core) with respect to the target. In the black disc model [17–21], the $S$-matrices for core and neutron scattering are given by

$$S_i(b_i) = 0, \quad |b_i| \leq R_t + R_i \qquad S_i(b_i) = 1, \quad |b_i| \geq R_t + R_i \qquad i = c, n, \tag{10}$$

where $R_c$ and $R_t$ are the r.m.s. radii of the core and the target nuclei respectively, while $R_n$ is the radius of the neutron. Note that the $S$-matrices depend neither on spin nor core variables. The longitudinal momentum distribution is obtained by integration of (9) over the two directions perpendicular to the beam axis. With a WF for the neutron-core relative motion from (2) together with the choice (10) for the $S$-matrices, the following expression is obtained for the longitudinal momentum distribution of the core fragment

$$\begin{aligned} \frac{d\sigma_{-n}}{dk_z} &= \sum_{ljJ_c} \frac{1}{2} \int_0^{R_t+R_n} b\, db \int_{R_c+R_t-b}^{\infty} r_\perp dr_\perp \int_{-\infty}^{\infty} dz \int_{-\infty}^{\infty} dz' f(r_\perp, b) \cdot \\ &\exp(ik_z(z-z')) \mathcal{R}^J_{ljJ_c}(\sqrt{r_\perp^2 + z^2}) \mathcal{R}^J_{ljJ_c}(\sqrt{r_\perp^2 + z'^2}) P_l\left(\frac{r_\perp^2 + zz'}{\sqrt{r_\perp^2 + z^2}\sqrt{r_\perp^2 + z'^2}}\right), \end{aligned} \tag{11}$$

where

$$f(r_\perp, b) = \begin{cases} 1 - \frac{1}{\pi} arccos\left(\frac{r_\perp^2 + b^2 - (R_c+R_t)^2}{2 r_\perp b}\right) & r_\perp < R_c + R_t + b \\ 1 & r_\perp > R_c + R_t + b, \end{cases} \tag{12}$$

when averaged over magnetic quantum numbers $M$. The functions $P_l$ are the Legendre polynomials. In this expression we have omitted the contribution from diffraction and Coulomb dissociation. The latter contribution should be negligible for light targets such as beryllium while the former gives a momentum distribution close to that obtained in nuclear stripping [21]. Finally the neutron stripping cross section is obtained by integrating Eq. (11) over longitudinal momentum,

$$\sigma_{-n} = \int \frac{d\sigma_{-n}}{dk_z} dk_z. \tag{13}$$

## 4. Dipole strength function and electromagnetic dissociation cross section

For a one-neutron halo nucleus the electromagnetic dissociation (EMD) cross section for $E1$ transitions can be calculated from [22]

$$\sigma_{EMD} = \int n^{E1}(E_\gamma)\sigma_\gamma^{E1}(E_\gamma)\frac{dE_\gamma}{E_\gamma}, \tag{14}$$

where the number of virtual photons is given by

$$n^{E1}(E_\gamma) = (2/\pi)Z_t^2\alpha(c/v)^2\left[\xi K_0(\xi)K_1(\xi) - (v^2\xi^2/2c^2)(K_1^2(\xi) - K_0^2(\xi))\right] \tag{15}$$

Here $\alpha$ is the fine structure constant, $Z_t$ the charge of the target nucleus, $v$ the speed of the projectile and $K_0$ ($K_1$) the modified Bessel function of zeroth (first) order with argument

$$\xi = \frac{E_\gamma}{\hbar v\gamma}\left(R + \frac{1}{2}\frac{\pi Z_p Z_t e^2}{\mu_{pt}v^2\gamma}\right) \quad ; \qquad R = r_0 A_t^{1/3} + R_p, \tag{16}$$

where $\mu_{pt}$ is the reduced mass of the projectile and the target, and $\gamma$ the relativistic factor. In Eq. (14) we took into account only the $E1$ multipolarity, which in our case is by far the dominant one.

The photo-dissociation cross section, $\sigma_\gamma^{E1}$, is simply related to the dipole strength function via

$$\frac{dB(E1;E_\gamma)}{dE_\gamma} = \frac{9\hbar c}{16\pi^3 E_\gamma}\sigma_\gamma^{E1}(E_\gamma). \tag{17}$$

For a valence neutron in $s$-wave relative motion to the core, the dipole strength function is given by [23]

$$\frac{dB(E1;E_\gamma)}{dE_\gamma} = \left(\frac{Z_p e}{A_p}\right)^2 \frac{3}{2\pi^2\hbar^3}\sqrt{2\mu^3(E_\gamma - S_n)}\,|A|^2, \tag{18}$$

and for a neutron in $d$-wave relative to the core

$$\frac{dB(E1;E_\gamma)}{dE_\gamma} = \left(\frac{Z_p e}{A_p}\right)^2 \frac{3}{2\pi^2\hbar^3}\sqrt{2\mu^3(E_\gamma - S_n)}\left(\frac{2}{5}|B|^2 + \frac{3}{5}|C|^2\right), \tag{19}$$

where the radial integrals are

$$A = \int_0^\infty dr r^3 j_1\left(\frac{1}{\hbar}\sqrt{2\mu(E_\gamma - S_n)}\, r\right)\mathcal{R}^J_{0jJ_c}(r), \tag{20}$$

$$B = \int_0^\infty dr r^3 j_1\left(\frac{1}{\hbar}\sqrt{2\mu(E_\gamma - S_n)}\, r\right)\mathcal{R}^J_{2jJ_c}(r), \tag{21}$$

$$C = \int_0^\infty dr r^3 j_3\left(\frac{1}{\hbar}\sqrt{2\mu(E_\gamma - S_n)}\, r\right)\mathcal{R}^J_{2jJ_c}(r). \tag{22}$$

Here $j_l$ are spherical Bessel functions while $\mathcal{R}^J_{ljJ_c}(r)$ is the radial part of the WF in the relative neutron-core coordinate, see Eq. (2).

## 5. Application to $^{19}$C and $^{17}$C

The $^{17}$C and $^{19}$C nuclei are the heaviest odd-neutron isotopes of carbon which are still stable against particle emission. They are both $\beta$-decaying with observed half lives of 174±31 ms [24] and 49±4 ms [25] respectively. Table 1 summarizes some basic ground state properties of the A=14-19 carbon isotopes. The spin/parity assignments of the $^{17}$C and $^{19}$C ground states are still not experimentally determined, but three closely spaced low-lying candidates $1/2^+$, $3/2^+$, $5/2^+$ are expected. The r.m.s. matter radii shown in the last column of Table 1 were extracted from the total reaction cross sections. Unfortunately, the only measurement of the reaction cross sections for $^{17,19}$C [27] suffered from low statistics and an experimental method which is not completely adequate for halo systems.

To qualitatively understand the structure of these nuclei we recall the route taken from $^{14}$C up to $^{19}$C by means of simple shell model considerations (see Table 1). Let us assume that the ($Z$=6) protons completely occupy the $0s_{\frac{1}{2}}$ and $0p_{\frac{3}{2}}$ subshells on the proton-side, and do not contribute to the total angular momenta of the ground states of these nuclei. A huge difference in single particle separation energies for the even and odd members of the pairs {$^{14}$C,$^{15}$C}, {$^{16}$C,$^{17}$C} and {$^{18}$C,$^{19}$C} suggests a *core+particle* cluster model as a first approximation for these even-odd nuclei. In general, this corresponds to core protons

and core neutrons occupying filled shells plus a single particle responsible for the total spin and parity of the system.

More realistically the $1s_{\frac{1}{2}}$, $0d_{\frac{5}{2}}$ and $0d_{\frac{3}{2}}$ orbits might be only partially filled. In order to go beyond the approximation of an inert core and a particle, there are two obvious alternatives. Either one includes more clusters from the very beginning or one takes core degrees of freedom into account. As an illustrative example, consider $^{11}$Be, where the first neutron is bound by 0.5 MeV, whereas it takes another 6.8 MeV to remove the next neutron. This last energy should be compared with the excitation energy of 3.4 MeV for the first $2_1^+$ state in $^{10}$Be [8]. Therefore coupling single particle states to the ground and low-lying excited states of the core seems to be a reasonable way to model the one-neutron halo nucleus $^{11}$Be. The low-lying $2_1^+$ states at 1.77 MeV and 1.62 MeV of $^{16}$C and $^{18}$C respectively motivate us to use such a model also for these particular systems.

### 5.1. $^{19}$C: the heaviest one-neutron halo nucleus so far?

The $^{19}$C nucleus is the most weakly bound odd carbon isotope, and its mass has been determined using time-of-flight techniques, from which a weighted average yields a one-neutron separation energy of $S_n$=242±95 keV [5]. Since this experimental quantity is not known with satisfactory accuracy it is treated as an input parameter in our CC equations (3), and uncertainty remains when our results are compared with available experimental data. Therefore we also performed calculations for a larger value, $S_n$=0.50 MeV, to investigate the sensitivity of the results to the separation energy.

Unfortunately there are not much data available to parameterize the *core-neutron* interaction within our model. Thus, selecting parameters for the potentials, the most frequently used quantities for the Woods-Saxon and its derivative from N∼Z nuclei, were chosen (see Eqs. (4,5) and Table 2). The excitation energy of the low-lying state of $^{18}$C, $E^*(2_1^+)$= 1.62±0.02 MeV, is taken from [7] and is used when coupling of a single particle states to the $2_1^+$ core state is taken into account. This coupling is generated only for a nonzero value of the deformation of the $^{18}$C core. The deformation is not experimentally known, but calculations [11] predict quite a large deformation, $\beta$ ∼0.5. We select $\beta$=0 and $\beta$=0.5 to demonstrate the sensitivity of the observables to this parameter. Further increase of the deformation parameter does not qualitatively change the picture. In a

previous letter [12], we used $\beta$=1.0 and the results were similar to the ones obtained here for $\beta$=0.5.

Since the spin/parity for the ground state of $^{19}$C is still experimentally unknown we have performed calculations assuming three possibilities for the ground state. A $J^{\pi}$=1/2$^{+}$ state involves three channels in our calculations as shown in Table 3, while $J^{\pi}$=3/2$^{+}$ and $J^{\pi}$=5/2$^{+}$ states only include the two dominant ones, see Tables 4 and 5. In this simplified picture it is easy to investigate the sensitivity of the results to parameters such as one-neutron separation energy, deformation parameter and spin-orbit force, which have not yet been satisfactory determined.

Calculated values of the r.m.s. neutron-core distance $R_{cn}$ show that the halo of $^{19}$C extends well beyond the $^{18}$C core in all these scenarios, and especially in the case of a $J^{\pi}$=1/2$^{+}$ ground state configuration, with the r.m.s. core size taken as $R_m^{core} \simeq r_o A^{\frac{1}{3}} \simeq$ 3.0 fm. Such an extended matter distribution should manifest itself as an enhancement of the total reaction cross section compared with neighbouring isotopes. The experimental r.m.s matter radius extracted from available experiment is $R_m$=2.74$\pm$0.96 fm, but obviously the error bars are much to large to say something definite concerning the size of $^{19}$C.

The longitudinal momentum distributions of $^{18}$C fragments from $^{19}$C breakup reactions, corresponding to our three model ground state wave functions, are presented in Figs. 1, 2 and 3 together with the data of [5,13]. We show the $J^{\pi}$=1/2$^{+}$, $J^{\pi}$=3/2$^{+}$ and the $J^{\pi}$=5/2$^{+}$ calculations with and without quadrupole coupling (see Tables 3, 4 and 5 for the runs). The calculated curves (11), with parameters $R_c$=3.0 fm, $R_t$=2.38 fm [28] and $R_n$=0.8 fm, have been normalized to best match the experimental points. Although the calculated full width half maximum (FWHM) differ by more than a factor of two (we return to this point), the available experimental information[1] (including the uncertainty in $S_n$) is not precise enough for a definite spin/parity assignment for the ground state of $^{19}$C. In all cases the widths are mainly determined by the $s$-wave components, since $d$-waves give FWHM values of the order 200 MeV/c, and therefore only influence the "background".

[1]We mention that the FWHM for neutrons [6] is 55 $\pm$ 15 MeV/c compared with 42 $\pm$ 4 MeV/c for $^{18}$C fragments [13] in the projectile rest frame.

In order to investigate further the sensitivity to the one-neutron separation energy in the case of a $J^\pi$=1/2$^+$ ground state, we also performed a calculation for the value $S_n(^{19}\mathrm{C})$=0.50 MeV (see run {1/2$^+$;0.50;0.50} in Table 3), i.e. larger than the upper limit set by the present error bars. This improves the $J^\pi$=1/2$^+$ fit to the momentum distribution data, see Fig. 4. We find that the FWHM value roughly scales as the square root of the one-neutron separation energy; a result which is exact for an s-wave neutron in a simple Yukawa wave-model. In the case of $J^\pi$=3/2$^+$ and $J^\pi$=5/2$^+$ the relevant separation energy (for an $s$-wave neutron) is that of the $[2_1^+ \otimes 1s_{\frac{1}{2}}; \frac{3}{2}^+]$ and $[2_1^+ \otimes 1s_{\frac{1}{2}}; \frac{5}{2}^+]$ components, i.e. the sum of $S_n(^{19}\mathrm{C})$ and the excitation energy $E_A^*(2_1^+)$=1.62 MeV in $^{18}$C, and essentially larger than for the g.s.$\rightarrow$g.s. coupling. Therefore as far as the $J^\pi$=3/2$^+$ and the $J^\pi$=5/2$^+$ configurations are concerned, the width of the longitudinal momentum distribution is not very sensitive to the one-neutron separation energy of $^{19}$C.

Inclusion of absorption in the reaction mechanism did not change the FWHM value very much in either realistic case (when the coupling is included) – only the distribution for large momenta is affected. This result is due to the predominance of $s$-wave so that a large fraction of the WF is well outside the core. This differs from the case of $^8$B, currently discussed as a potential one-proton halo candidate, where the valence proton is mainly bound in a $p_{3/2}$ orbit. Here the centrifugal ($l$=1) as well as the Coulomb barrier limit the extension of the proton-orbit. It was recently shown [18,21] that for $^8$B the effect of absorption reduces the FWHM value by about 50%.

In Tables 3, 4 and 5, we also present the neutron stripping cross sections, $\sigma_{-n}$, obtained from Eq. (13). The run {1/2$^+$;0.50;0.24} overestimates the neutron stripping cross section. The experimental value agrees in fact better with a $J^\pi$=3/2$^+$ or 5/2$^+$ assignment taking into account that our calculated value of $\sigma_{-n}$ serves as a *lower limit* for comparison with experiment, as data must also contain the contribution from diffraction dissociation. Thus, based only on the available experimental longitudinal momentum distribution and neutron stripping cross section we are not able to select definitely the ground state configuration.

There are additional important points which have to be mentioned here. A deformation of $\beta \sim$0.5 is already sufficient to account for $J^\pi$=3/2$^+$ as the spin/parity assignments of the ground state of $^{19}$C. The mixing of the single $s$-wave neutron to the $2_1^+$ exited

state of $^{18}$C is indispensable in this particular case. The $J^\pi$=5/2$^+$ ground state wave function gives too broad momentum distribution, due to the lack of $s$-wave strength. However, for a small spin-orbit interaction the $s$-wave contribution increases significantly and the resulting momentum distributions for the $J^\pi$=3/2$^+$ and the $J^\pi$=5/2$^+$ scenario looks very similar and they both give reasonable fits to the data points, see Figs. 2 and 3. In conclusion, a $J^\pi$=1/2$^+$ or a $J^\pi$=3/2$^+$ ground state looks preferable based only on available $^{18}$C momentum distribution, and a $J^\pi$=5/2$^+$ ground state can be possible only for an abnormally small spin-orbit interaction. On the other hand, the spin-orbit strength does not matter if we assume the $J^\pi$=1/2$^+$ scenario; here the $[0^+ \otimes 1s_{\frac{1}{2}}; \frac{1}{2}^+]$ coupling is dominant, and the spin-orbit force acts only via the $[2_1^+ \otimes 0d_{\frac{5}{2}}; \frac{1}{2}^+]$ branch which is of minor importance in this particular case.

The different candidates for the ground state configuration of $^{19}$C should have very different Coulomb dissociation cross sections. As already discussed in [4] for the case of $^{11}$Be, the halo formation produces significant effects on the direct Coulomb dissociation, because the $p$-wave continuum states are strongly connected by $E1$ transition with the $s$-orbit of the halo. The corresponding calculated transition strengths for Coulomb dissociation of $^{19}$C obtained from Eqs. (18) and (19) are presented in Fig. 5 for all three possible ground state configurations; $J^\pi$=1/2$^+$ (the two curves for this configuration correspond to two different separation energies 0.24 MeV and 0.50 MeV), $J^\pi$=3/2$^+$ and $J^\pi$=5/2$^+$. The different assumptions for the ground state of $^{19}$C lead to completely different behaviours of the $dB(E1;E_\gamma)/dE_\gamma$ dependence both in magnitude and position of the maximum. Although the uncertainty in the $S_n(^{19}\mathrm{C})$ value implies a corresponding uncertainty in the peak position (see curves $\{1/2^+; 0.50; 0.24\}$ and $\{1/2^+; 0.50; 0.50\}$), the difference between $J^\pi$=1/2$^+$ and $J^\pi$=3/2$^+$ ($J^\pi$=5/2$^+$) is outstanding. The EMD cross sections are given in Tables 3, 4 and 5 and have been calculated from Eq. (14) using the strength function shown in Fig. 5 and a spectrum of virtual photons corresponding to a $^{19}$C beam at 77 MeV/u (30 MeV/u) on a tantalum target. For such experimental conditions, preliminary data show a cross section of 1.1±0.4 b [13] (0.8±0.3 b [30]). However, one should keep in mind that these experimental cross sections include nuclear as well as Coulomb breakup. All runs mentioned above give in principle three different

cross sections, but we have to await more precise experimental data, before drawing the conclusion on the structure of $^{19}$C. However, as shown above, the transition strengths and EMD cross sections may be decisive for selecting the best candidate of $^{19}$C, due to the large sensitivity to the ground state structure.

### 5.2. The ground state structure of $^{17}$C

Data concerning the structure of the $^{17}$C nucleus is quite poor and can easily be summarized in a few sentences [31]. As already given in Table 1, the $^{17}$C nucleus is stable with respect to $^{16}$C+n by 0.73 MeV. Observation of $\beta$-delayed neutron emission has been reported [24]. An excited state of $^{17}$C is observed at $E_{ex}$=295±20 keV. The longitudinal momentum distributions of $^{16}$C fragments, FWHM=94±19 MeV/c, and the neutron stripping cross sections, $\sigma_{-n}$=40.9±4.3 mb, from $^{17}$C breakup reactions at 83 MeV/u on a beryllium target have been measured and published [5]. The experiment was later improved and new values for the longitudinal momentum width and neutron stripping cross section have been extracted [13], namely FWHM=145±5 MeV/c and $\sigma_{-n}$=25.6±0.7 mb. All data points shown in the Figs. in this section correspond to this latest measurement.

Three closely spaced low-lying states are expected again like for the $^{19}$C case, i.e. $J^{\pi}$=1/2$^{+}$, 3/2$^{+}$, 5/2$^{+}$, and it is not clear which one of them is the ground state. Nevertheless, based on the systematics described in [32], where a modified Millener-Kurath interaction is employed within the shell model formalism, it is unlikely that $^{17}$C has a $J^{\pi}$=5/2$^{+}$ ground state. Moreover, analysis of the $\gamma$-ray spectra following the $\beta$-decay of $^{17}$C does not support 5/2$^{+}$ as the ground state spin either [32]. Unfortunately, as is clearly stated in [32], the present shell model calculations cannot give a definitive prediction for the ground state spin of $^{17}$C, and 1/2$^{+}$ and 3/2$^{+}$ both remain viable possibilities.

On the other hand, in [10], where shell model interactions are constructed in the cross-shell model space connecting the 0$p$ and 1$s$0$d$ shells with the perturbative effect of the neighbouring 0$s$ and 0$f$1$p$ shells, only $J^{\pi}$=3/2$^{+}$ is left as a possibility for the spin/parity assignment of the $^{17}$C ground state. The relativistic mean field calculation [11] also predicts $J^{\pi}$=3/2$^{+}$.

The parameterization procedure of the $^{16}$C core and the single neutron interaction within our *core+particle* model is again taken similar to the case of the $^{19}$C calculations

(see Table 6). The excitation energy $E^*(2_1^+)$=1.766±0.01 MeV of the low lying state of the $^{16}$C nucleus is taken from [31].

The results of numerical calculations with the assumption of a $J^\pi$=$1/2^+$ ground state are given in Table 7. It is clear that the obtained FWHM underestimates the corresponding value extracted from the experiment as shown in Fig. 6. Inclusion of quadrupole coupling (see run $\{1/2^+;0.55;0.73\}$ in Table 7) by the ordinary procedure assuming that the neutron-rich $^{16}$C core is deformed, makes the momentum distribution a little broader, but still inconsistent with data. Note here the difference from the calculations in previous section where the $\beta$ parameter of $^{18}$C is experimentally unknown. The value $\beta$=0.55 can be estimated from Eq. (7) with the experimental transition probability $B(E2 : 0_{gs}^+ \rightarrow 2_1^+)$=40 e$^2$fm$^4$ [33] for the $^{16}$C nucleus. Similar values of deformations were predicted in [11].

The model is able to provide us with more favourable results for $J^\pi$=$1/2^+$ if the coupling $[2_1^+ \otimes 0d_{\frac{5}{2}}; \frac{1}{2}^+]$ becomes dominant ($\sim$ 50%). This is possible if either *i*) a very large deformation parameter ($\beta$ ~1.0) is used; or *ii*) a less realistic spin-orbit potential strength is implemented ($V_{so}$ ~15.0 MeV); or *iii*) the combination of both *i* and *ii* is employed. In spite of the fact that the desired FWHM is nearly guaranteed (it is still narrower anyway), the total momentum distribution is poorly reproduced for higher momenta – the distribution becomes too broad. Since now the momentum distribution is not vanishing in the region of momentum 100 – 200 MeV/c (because of the quite strong *d*-wave contribution) it becomes clear that the momentum itself is characterized not only in the peak region but also in the tails.

Before any conclusions on the validity of the model and/or the structure of the ground state of $^{17}$C are drawn, we also check other possibilities, i.e. $J^\pi$=$3/2^+$ and $J^\pi$=$5/2^+$ for the ground state. Again like for $^{19}$C, calculations without any coupling (see runs $\{3/2^+;0.00;0.73\}$ and $\{5/2^+;0.00;0.73\}$ in Tables 8 and 9) overestimate the width of momentum distribution giving FWHM>200 MeV/c. If the admixture of $[2_1^+ \otimes 1s_{\frac{1}{2}}; \frac{3}{2}^+]$ (or $[2_1^+ \otimes 1s_{\frac{1}{2}}; \frac{5}{2}^+]$) coupling becomes dominant with asymptotic decay for the corresponding form factor governed by the energy $E_A^B = S_n + E_A^*(2_1^+)$, then the calculated FWHM is larger then 80 MeV/c. Numerical results (runs $\{3/2^+;0.55;0.73\}$ and $\{5/2^+;0.55;0.73\}$) for

$\beta$=0.55 are given in Tables 8 and 9 with corresponding longitudinal momentum distributions presented in Figs. 7 and 8. As one could easily expect, both runs $\{3/2^+; 0.55; 0.73\}$ and $\{5/2^+; 0.55; 0.73)\}$ give very similar results when the spin-orbit force is switched off. On the other hand, if the usual spin-orbit strength $V_{so} \sim 6.5$ MeV is present, we are able to distinguish these two scenarios. For the run $\{5/2^+; 0.55; 0.73\}$ the longitudinal momentum distribution becomes broader than for $\{3/2^+; 0.55; 0.73\}$. Such a behaviour can be understood if we recall the $0d$ orbit splitting into $0d_{\frac{3}{2}}$ and $0d_{\frac{5}{2}}$; $0d_{\frac{3}{2}}$ is closer to $1s_{\frac{1}{2}}$ if compared with $0d_{\frac{5}{2}}$. Therefore, in the latter case the $[0^+_{gs} \otimes 0d_{\frac{5}{2}}; \frac{5}{2}^+]$ coupling becomes dominant giving wider momentum distribution, while increase of the $[0^+_{gs} \otimes 0d_{\frac{3}{2}}; \frac{3}{2}^+]$ form factor is not so noticeable (see Tables 8 and 9) in the presence of the spin-orbit interaction. In other words, our model suggests a possibility to distinguish in between $J^\pi$=$3/2^+$ and $J^\pi$=$5/2^+$ if more precise experimental data becomes available. Guided by the results from other calculations where a $J^\pi$=$3/2^+$ ground state is preferable, we conclude that in such a scenario the deformation parameter must be smaller than what we obtain from the $B(E2)$ value. With the value $\beta \sim$0.2 we obtain good agreements for the longitudinal momentum distribution, see Table 8 and Fig. 7.

Like for $^{19}$C, we also present some predictions for the neutron stripping cross sections and EMD cross sections for different scenarios as shown in Tables 7, 8 and 9. The different EMD cross sections for $J^\pi$=$1/2^+$ and $J^\pi$=$3/2^+$ (or $J^\pi$=$5/2^+$) is clearly seen, but unfortunately there are no experimental data available for comparison.

At this stage we can conclude that more precise experimental information about $^{17}$C is definitively needed for a more realistic calculation of this nucleus. It might be that the valence neutron does not behave as a weakly bound halo particle well separated from the core, and may mix in many states of $^{16}$C that have not been taken into account. Nevertheless, $s$-motion of the valence neutron is predicted with considerable ($\sim$50%) admixture either from $[2^+_1 \otimes 1s_{\frac{1}{2}}; \frac{3}{2}^+]$ or from $[2^+ \otimes 1s_{\frac{1}{2}}; \frac{5}{2}^+]$ coupling. Based on the available experimental momentum distribution alone, it is reasonable to rule out $J^\pi$=$1/2^+$ as the ground state of $^{17}$C.

## 6. $^{15}$C: a challenge for the *core+particle* cluster model?

The $^{15}$C nucleus has an abnormal ground state, $J^{\pi}=1/2^{+}$, with a spectroscopic factor $S$=0.88 for the relative $s$-motion of a single neutron with respect to the $^{14}$C core [34]. The single-neutron separation energy $S_n(^{15}\mathrm{C})$=1.218 MeV [34] is quite small as well. The longitudinal momentum distribution of $^{14}$C fragments from $^{15}$C breakup reactions at 83 MeV/u [13] have been found to be narrow on a beryllium target as well as on a tantalum target with FWHM values 67±2 MeV/c and 67±1 MeV/c respectively. From this information only, $^{15}$C have all the necessary ingredients typically for halo-systems. The $^{14}$C nucleus is expected to be spherical due to the magic number $N$=8, what is also predicted in Ref. [11]. For $^{15}$C a $\beta$ of 0.3 is suggested [11]. Moreover, from $^{14}$C to $^{22}$C, the deformation increases gradually up to the maximum for $^{18}$C and then decreases to zero for $^{22}$C [11]. Similar results were reported from the so called antisymmetrized molecular dynamics calculations [35]. On the other hand, $B(E2;0^{+}_{gs} \rightarrow 2^{+}_{1})$=18.2 e$^2$fm$^4$ value for $^{14}$C is known [33], and it gives the deformation $\beta \sim 0.4$ if Eq. (7) is applied. However, in this particular case, the $2^{+}_{1}$ state of $^{14}$C at $E^{*}_{A}(2^{+}_{1}) = 7.01$ MeV with respect to the ground state $0^{+}$ is not the lowest one [34] as we had for $^{16,18}$C.

The application of the *particle+core* coupling model for $^{15}$C might be questionable, but inclusion of the $[2^{+}_{1} \otimes 0d_{\frac{5}{2}}; \frac{1}{2}^{+}]$ coupling with $\beta \sim 0.4$ reproduces the spectroscopic factor extracted from the experiment as represented in Table 11. In addition, we calculate similar observables as for the $^{17,19}$C nuclei to be compared with preliminary experimental data [13]. The inclusion of quadrupole coupling does not practically change the longitudinal momentum distribution as shown in Fig. 9, but we fail badly both in $\sigma_{-n}$ and $\sigma_{E1}$ cross sections (see Table 11).

There is one more thing which has to be mentioned; the situation for the r.m.s. matter radius of $^{15}$C is quite complicated as well. In Ref. [28], $^{15}$C has even slightly smaller r.m.s. radius than $^{14}$C, which is in contradiction with our obtained results. On the other hand, the authors in [26] argue for an increment of the r.m.s. radius if one adds one more neutron to $^{14}$C. We refer the reader to Tables 1 and 11 for exact numbers.

At this stage we have to admit that direct application of the *particle+core* cluster model does not seem to be a good approach to the ground state calculation of $^{15}$C. However,

available data should be confirmed first before we can draw more definite conclusions.

## 7. Summary

The question about the halo nature of $^{19}$C and its underlying structure is one of the interesting current questions in dripline physics. We have tried to elucidate this question by solving CC equations for a single neutron interacting with a deformed core in a *particle+core* cluster model. In this two-cluster picture, the halo states are viewed as composed of translational invariant overlaps with low-lying core states. Thus we have, within a non-adiabatic *particle-rotor* model with axial symmetry, studied to what extent the core geometry and core degrees of freedom are reflected in the properties of the $^{19}$C system.

Overlap functions, longitudinal momentum distributions, *r.m.s.* radii were calculated as well as neutron stripping cross sections and EMD cross sections both for $^{19}$C and for $^{17}$C. Model predictions for the dipole strength functions $dB(E1;E_\gamma)/dE_\gamma$ were presented as well. The results were compared with the sparse available data.

The conclusion is that $^{19}$C seems to qualify as another one-neutron halo nucleus with essential contribution from relative $s$-motion between halo neutron and core, with the core, $^{18}$C, either in its $0^+$ ground state or in the $2^+$ excited state giving $J^\pi$=$1/2^+$ or $J^\pi$=$3/2^+$ (or $J^\pi$=$5/2^+$) respectively for the $^{19}$C ground state. On the other hand, $J^\pi$=$1/2^+$ is ruled out in case of the $^{17}$C nucleus. Available data do not allow a clear discrimination between spin/parity assignments for the ground state of these loosely bound carbon isotopes.

In order to verify our model where core degrees of freedom are taken into account, we suggest a measurement where the core fragment is registrated in coincidence with a $\gamma$-ray originating from the deexcitation of the core. Such a measurement could clearify the whole picture and provide additional and very important information.

Finally, we again want to stress that in order to determine the structure and quantum numbers of these nuclei the following quantities should be measured or remeasured with higher precision, namely the longitudinal momentum distribution of the core, the electromagnetic cross section at different energies and the one-neutron separation energy of $^{19}$C. In addition, a better measurement of the reaction cross section would provide us with a

more precise size of these nuclei.

## 8. Acknowledgments

One of the authors, (D.R), thanks the hospitality of the University of Bergen and the Chalmers University of Technology and Göteborg University where most of the work was performed, and for support in part from Nordplus and the Western Norway TP for the EU Leonardo da Vinci Placement Grant. The authors greatly acknowledge discussions with D. Bazin, N.A. Orr and B.M. Sherrill.

## REFERENCES


1. F.M. Nunes, I.J. Thompson and R.C. Johnson, Nucl. Phys. A 596 (1995) 171.
2. H. Esbensen, B.A. Brown and H. Sagawa, Phys. Rev. C 51 (1995) 1274.
3. N.Vinh Mau, Nucl. Phys. A 592 (1995) 33.
4. D. Ridikas and J. S. Vaagen, ECT* preprint #: ECT*-96-006, 6 (1996).
5. D. Bazin *et al.*, Phys. Rev. Lett. 74 (1995) 3569.
6. F.M. Marques *et al.*, Phys. Lett. B 381 (1996) 407.
7. D.R. Tilley, H.R. Weller and C.M. Cheves, Nucl. Phys. A 595 (1995) 1.
8. F. Ajzenberg-Selove, Nucl. Phys. A 490 (1988) 1.
9. K. Riisager, A.S. Jensen and P. Møller, Nucl. Phys. A 548 (1992) 393.
10. E.K. Warburton and B.A. Brown, Phys. Rev. C 46 (1992) 923.
11. Ren Zhongzhou, Z.Y. Zhu, Y.H. Cai and Xu Gongou, Nucl. Phys. A 605 (1996) 75.
12. D. Ridikas, M.H. Smedberg, J.S. Vaagen and M.V. Zhukov, Europhys. Lett. 37 (1997) 385.
13. B. Sherrill, private communication (1996).
14. G. Audi and A.H. Wapstra, Nucl. Phys. A 565 (1993) 1.
15. A. Bohr and B. Mottelson, Volumes 1-2, Nuclear Structure(Benjamin, Reading, 1969).
16. J.M. Bang, F.G. Gareev, W.J. Pinkston and J.S. Vaagen, Phys. Rep. 125 (1985) 255.
17. R. Serber, Phys Rev. 72 (1947) 1008.
18. H. Esbensen, Phys. Rev. C 53 (1996) 2007.
19. H. Sagawa and N. Takigawa, Phys Rev. C 50 (1994) 985.
20. F. Barranco, E. Vigezzi and R.A. Broglia, Z. Phys. A 356 (1996) 45.
21. P.G. Hansen, Phys. Rev. Lett., 77 (1996) 1016.
22. C.A. Bertulani, L.F. Canto, M.S. Hussein, Phys. Rep. 226 (1993) 281.
23. D.M. Kalassa and G. Baur, J. Phys. G: Nucl. Part. Phys. 22 (1996) 115.
24. P.L. Reeder *et. al.* Phys Rev. C 44 (1991) 1435.
25. J.P. Dufour *et. al.* Phys. Lett. B 206 (1988) 195.
26. E. Liatard et. al. Europhys. Lett. **13** (1990) 401.
27. M.-G. Saint-Laurent et. al., Z. Phys Z 332 (1989) 457.
28. I. Tanihata *et. al.*, Phys. Lett. B 206 (1988) 592.

29. D. Bazin et al., Gull Lake Conf. on Nucl. Phys. Near the Driplines, Michigan (1996).

30. E. Liegard, N. Orr et al., in preparation.

31. D.R. Tilley, H. R. Weller and C. M. Cheves, Nucl. Phys. A 564 (1993) 1.

32. E.K. Warburton and D. J. Millener, Phys. Rev. C 39 (1989) 1120.

33. S. Raman *et al.*, At. Data Nucl. Data Tables 42 (1989) 1.

34. F. Ajzenberg-Selove, Nucl. Phys. A 523 (1991) 1.

35. H. Horiuchi, International Summer School, NATO Advanced Study Institute, Dronten, (1996).

Figure 1. Longitudinal momentum distribution of $^{18}$C fragments from $^{19}$C ($J^{\pi}$=1/2$^{+}$) breakup reactions. The experimental data are taken at 77 MeV/u on a beryllium target [13].

Figure 2. Longitudinal momentum distribution of $^{18}$C fragments from $^{19}$C ($J^{\pi}$=3/2$^{+}$) breakup reactions. The experimental data are taken at 77 MeV/u on a beryllium target [13].

Figure 3. Longitudinal momentum distribution of $^{18}$C fragments from $^{19}$C ($J^{\pi}$=5/2$^{+}$) breakup reactions. The experimental data are taken at 77 MeV/u on a beryllium target [13].

Figure 4. Longitudinal momentum distribution of $^{18}$C fragments from $^{19}$C ($J^{\pi}$=1/2$^{+}$, $S_n$=0.50 MeV) breakup reactions. The experimental data are taken at 77 MeV/u on a beryllium target [13].

Figure 5. The $E1$ strength function for different $^{19}$C ground state configurations.

Figure 6. Longitudinal momentum distribution of $^{16}$C fragments from $^{17}$C ($J^{\pi}$=1/2$^{+}$) breakup reactions. The experimental data are taken at 83 MeV/u on a beryllium target [13].

Figure 7. Longitudinal momentum distribution of $^{16}$C fragments from $^{17}$C ($J^{\pi}$=3/2$^{+}$) breakup reactions. The experimental data are taken at 83 MeV/u on a beryllium target [13].

Figure 8. Longitudinal momentum distribution of $^{16}$C fragments from $^{17}$C ($J^{\pi}$=5/2$^{+}$) breakup reactions. The experimental data are taken at 83 MeV/u on a beryllium target [13].

Figure 9. Longitudinal momentum distribution of $^{14}$C fragments from $^{15}$C ($J^{\pi}$=1/2$^{+}$) breakup reactions. The experimental data are taken at 83 MeV/u on a beryllium target [13].

Table 1

The ground state structure of the $A = 14 - 19$ carbon isotopes. The experimental r.m.s matter radii [26] are extracted from the experiment [27].

| Nucleus | $J^\pi$ | $T_z$ | $S_n$ (MeV) | $R_m$ (fm) |
|---|---|---|---|---|
| $^{14}$C | $0^+$ | 1 | 8.1765 | 2.62±0.06 |
| $^{15}$C | $1/2^+$ | 3/2 | 1.2181 | 2.78±0.09 |
| $^{16}$C | $0^+$ | 2 | 4.251 | 2.76±0.06 |
| $^{17}$C | $(1/2^+,3/2^+,5/2^+)$ | 5/2 | 0.729±0.018 | 3.04±0.11 |
| $^{18}$C | $0^+$ | 3 | 4.188 | 2.90±0.19 |
| $^{19}$C | $(1/2^+,3/2^+,5/2^+)$ | 7/2 | 0.242±0.095 | 2.74±0.96 |

Table 2

Parameters used in the calculation for the $^{18}$C+n system.

| $S_n$ (MeV) | $E^*(2_1^+)$ (MeV) | $R_o$ (fm) | $a$ (fm) | $V_{so}$ (MeV) | $\beta$ |
|---|---|---|---|---|---|
| 0.242 and 0.500 | 1.62 | 3.00 | 0.65 | 6.50 | 0.00 and 0.50 |

Table 3

Results of calculations for the ground state of $^{19}$C with $J^{\pi}$=1/2$^{+}$ ($S_n$=0.24 MeV and $S_n$=0.50 MeV). The calculated matter radii for the runs $\{1/2^{+}; 0.00; 0.24\}$, $\{1/2^{+}; 0.50; 0.24\}$, $\{1/2^{+}; 0.00; 0.50\}$ and $\{1/2^{+}; 0.50; 0.50\}$ are $R_m$=3.57 fm, $R_m$=3.50 fm, $R_m$=3.33 fm, and $R_m$=3.28 fm respectively when all channels are taken into account. The $\Gamma$=FWHM values in the case of absorption have been calculated according to equation (11) with parameters $R_t$=2.38 fm [28], $R_c$=3.00 fm and $R_n$=0.8 fm. The experimental value is FWHM=42±4 MeV/c [13]. The extracted $\sigma_{-n}$ and $\sigma_{E1}$ values are 105±17 mb [5] and 1.1±0.4 b [13] (0.8±0.3 b [30]) respectively. The EMD cross section is calculated on a $^{181}$Ta target at 77 (30) MeV/u with parameters $R_t$=1.25·A$^{1/3}$ fm and $R_p$=3.50 fm.

| Run $\{J^{\pi}; \beta; S_n\}$ | Channel $[J_c \otimes j]$ | Weight (%) | $R_{cn}$ (fm) | $\Gamma^{Serb.}$ (MeV/c) | $\Gamma^{Absorp.}$ (MeV/c) | $\sigma_{-n}$ (mb) | $\sigma_{E1}$ (mb) |
|---|---|---|---|---|---|---|---|
| $\{1/2^{+}; 0.00; 0.24\}$ | $[0^{+} \otimes 1s_{\frac{1}{2}}]$ | 100 | 9.21 | 33 | 31.6 | 162.8 | 3179 (5968) |
| $\{1/2^{+}; 0.50; 0.24\}$ | $[0^{+} \otimes 1s_{\frac{1}{2}}]^2$ | 84 | 9.23 | 33 | 31.5 | 136.5 | 2688 (5051) |
| $\{1/2^{+}; 0.50; 0.24\}$ | $[2^{+} \otimes 0d_{\frac{3}{2}}]$ | 2 | 4.27 | 266 | 210.5 | 1.0 | 1.2 (1.2) |
| $\{1/2^{+}; 0.50; 0.24\}$ | $[2^{+} \otimes 0d_{\frac{5}{2}}]$ | 14 | 4.12 | 276 | 212.2 | 7.3 | 8.7 (8.1) |
| $\{1/2^{+}; 0.50; 0.24\}$ | 3 channels | 100 | 8.62 | 34 | 31.8 | 144.8 | 2698 (5060) |
| $\{1/2^{+}; 0.00; 0.50\}$ | $[0^{+} \otimes 1s_{\frac{1}{2}}]$ | 100 | 7.2 | 44 | 41.7 | 131.5 | 1379 (2345) |
| $\{1/2^{+}; 0.50; 0.50\}$ | $[0^{+} \otimes 1s_{\frac{1}{2}}]$ | 76 | 7.18 | 44 | 41.6 | 99.6 | 1055 (1798) |
| $\{1/2^{+}; 0.50; 0.50\}$ | $[2^{+} \otimes 0d_{\frac{3}{2}}]$ | 3 | 4.20 | 271 | 214.4 | 1.4 | 1.5 (1.3) |
| $\{1/2^{+}; 0.50; 0.50\}$ | $[2^{+} \otimes 0d_{\frac{5}{2}}]$ | 21 | 4.05 | 282 | 216.2 | 10.4 | 11.0 (9.6) |
| $\{1/2^{+}; 0.50; 0.50\}$ | 3 channels | 100 | 6.57 | 47 | 42.5 | 111.4 | 1068 (1809) |

Table 4

Results of calculations for the ground state of $^{19}$C with $J^{\pi}=3/2^{+}$ and $S_n=0.24$ MeV. The calculated matter radii for the runs $\{3/2^{+};0.00;0.24\}$ and $\{3/2^{+};0.50;0.24\}$ are $R_m=3.07$ fm and $R_m=3.10$ fm respectively when all channels are taken into account. Calculations are presented with usual-spin orbit force $V_{so}=6.5$ MeV (above) and small spin-orbit force $V_{so}=0.5$ MeV (below).

| Run | Channel | Weight | $R_{cn}$ | $\Gamma^{Serb.}$ | $\Gamma^{Absorp.}$ | $\sigma_{-n}$ | $\sigma_{E1}$ |
|---|---|---|---|---|---|---|---|
| $\{J^{\pi};\beta;S_n\}$ | $[J_c\otimes j]$ | (%) | (fm) | (MeV/c) | (MeV/c) | (mb) | (mb) |
| $\{3/2^{+};0.00;0.24\}$ | $[0^{+}\otimes 0d_{\frac{3}{2}}]$ | 100 | 4.22 | 263 | 177.7 | 49.0 | 185.9 (279.5) |
| $\{3/2^{+};0.50;0.24\}$ | $[2^{+}\otimes 1s_{\frac{1}{2}}]$ | 49 | 4.96 | 72 | 68.1 | 38.8 | 120.8 (137.6) |
| $\{3/2^{+};0.50;0.24\}$ | $[0^{+}\otimes 0d_{\frac{3}{2}}]$ | 51 | 4.23 | 265 | 176.5 | 25.0 | 96.1 (144.8) |
| $\{3/2^{+};0.50;0.24\}$ | 2 channels | 100 | 4.60 | 92 | 82.8 | 63.8 | 216.9 (282.4) |
| $V_{so}=0.5$ MeV | | | | | | | |
| $\{3/2^{+};0.50;0.24\}$ | $[2^{+}\otimes 1s_{\frac{1}{2}}]$ | 71 | 4.99 | 70 | 67.9 | 57.3 | 178.7 (204.0) |
| $\{3/2^{+};0.50;0.24\}$ | $[0^{+}\otimes 0d_{\frac{3}{2}}]$ | 29 | 4.12 | 271 | 177.8 | 13.3 | 50.4 (75.8) |
| $\{3/2^{+};0.50;0.24\}$ | 2 channels | 100 | 4.75 | 78 | 73.2 | 70.6 | 229.1 (279.8) |

Table 5

Results of calculations for the ground state of $^{19}$C with $J^{\pi}=5/2^{+}$ and $S_n$=0.24 MeV. The calculated matter radii for the runs $\{5/2^{+};0.00;0.24\}$, $\{5/2^{+};0.50;0.24\}$ and are $R_m$=3.08 fm and $R_m$=3.10 fm respectively when all channels are taken into account. The calculations are presented with usual spin-orbit force $V_{so}$=6.5 MeV (above) and small spin-orbit force $V_{so}$=0.5 MeV (below).

| Run | Channel | Weight | $R_{cn}$ | $\Gamma^{Serb.}$ | $\Gamma^{Absorp.}$ | $\sigma_{-n}$ | $\sigma_{E1}$ |
|---|---|---|---|---|---|---|---|
| $\{J^{\pi};\beta;S_n\}$ | $[J_c \otimes j]$ | (%) | (fm) | (MeV/c) | (MeV/c) | (mb) | (mb) |
| $\{5/2^{+};0.00;0.24\}$ | $[0^{+} \otimes 0d_{\frac{5}{2}}]$ | 100 | 4.38 | 257 | 176.7 | 54.0 | 206.4 (311.0) |
| $\{5/2^{+};0.50;0.24\}$ | $[2^{+} \otimes 1s_{\frac{1}{2}}]$ | 22 | 4.58 | 72 | 66.8 | 15.1 | 46.8 (54.0) |
| $\{5/2^{+};0.50;0.24\}$ | $[0^{+} \otimes 0d_{\frac{5}{2}}]$ | 78 | 4.69 | 240 | 173.0 | 49.7 | 197.1 (298.9) |
| $\{5/2^{+};0.50;0.24\}$ | 2 channels | 100 | 4.67 | 194 | 122.2 | 64.7 | 243.9 (352.9) |
| $V_{so}$=0.5 MeV | | | | | | | |
| $\{5/2^{+};0.50;0.24\}$ | $[2^{+} \otimes 1s_{\frac{1}{2}}]$ | 73 | 4.99 | 72 | 68.0 | 59.2 | 184.5 (210.4) |
| $\{5/2^{+};0.50;0.24\}$ | $[0^{+} \otimes 0d_{\frac{5}{2}}]$ | 27 | 4.01 | 280 | 179.0 | 11.42 | 42.9 (64.3) |
| $\{5/2^{+};0.50;0.24\}$ | 2 channels | 100 | 4.75 | 78 | 72.4 | 70.6 | 227.4 (274.7) |

Table 6

Parameters used in the calculation for the $^{16}$C+n system.

| $S_n$ (MeV) | $E^{*}(2^{+}_{1})$ (MeV) | $R_o$ (fm) | $a$ (fm) | $V_{so}$ (MeV) | $\beta$ |
|---|---|---|---|---|---|
| 0.729 | 1.766 | 2.82 | 0.65 | 6.50 | 0.00, 0.20 and 0.55 |

Table 7

Results of calculations for the ground state of $^{17}$C with $J^{\pi}$=1/2$^{+}$ and $S_n$=0.73 MeV [31]. The calculated matter radius for the run $\{1/2^{+}; 0.00; 0.73\}$ is $R_m$=3.11 fm, while the run $\{1/2^{+}; 0.55; 0.73\}$ with all channels gives $R_m$=3.06 fm. The Γ=FWHM values in the case of absorption have been calculated according to equation (11) with parameters $R_t$=2.38 fm [28], $R_c$=2.82 fm and $R_n$=0.8 fm. The experimental value is FWHM=145±5 MeV/c [13] and FWHM=94±19 MeV/c [5]. The extracted $\sigma_{-n}$ value is 25.6±0.7 mb [13] and 40.9±4.3 mb [5]. The EMD cross section is calculated on a $^{181}$Ta target at 83 MeV/u with parameters $R_t$=1.25·$A_t^{1/3}$ fm, $R_p$=3.0 fm.

| Run $\{J^{\pi}; \beta; S_n\}$ | Channel $[J_c \otimes j]$ | Weight (%) | $R_{cn}$ (fm) | $\Gamma^{Serb.}$ (MeV/c) | $\Gamma^{Absorp.}$ (MeV/c) | $\sigma_{-n}$ (mb) | $\sigma_{E1}$ (mb) |
|---|---|---|---|---|---|---|---|
| $\{1/2^{+}; 0.00; 0.73\}$ | $[0^{+} \otimes 1s_{\frac{1}{2}}]$ | 100 | 6.31 | 52 | 48.7 | 120.4 | 1055 |
| $\{1/2^{+}; 0.55; 0.73\}$ | $[0^{+} \otimes 1s_{\frac{1}{2}}]$ | 74 | 6.31 | 52 | 48.2 | 88.6 | 786.6 |
| $\{1/2^{+}; 0.55; 0.73\}$ | $[2^{+} \otimes 0d_{\frac{3}{2}}]$ | 3 | 4.04 | 284 | 227.0 | 1.8 | 1.8 |
| $\{1/2^{+}; 0.55; 0.73\}$ | $[2^{+} \otimes 0d_{\frac{5}{2}}]$ | 23 | 3.88 | 294 | 229.2 | 11.5 | 11.7 |
| $\{1/2^{+}; 0.55; 0.73\}$ | 3 channels | 100 | 5.79 | 54 | 49.7 | 101.8 | 800.1 |

Table 8

Results of calculations for the ground state of $^{17}$C with $J^{\pi}=3/2^{+}$. The calculated matter radius for the run $\{3/2^{+};0.00;0.73\}$ is $R_m$=2.88 fm, while the run $\{3/2^{+};0.55;0.73\}$ with all channels gives $R_m$=2.91 fm. The calculations are presented with usual spin-orbit force $V_{so}$=6.5 MeV (above) and small spin-orbit force $V_{so}$=0.5 MeV (below).

| Run $\{J^{\pi};\beta;S_n\}$ | Channel $[J_c \otimes j]$ | Weight (%) | $R_{cn}$ (fm) | $\Gamma^{Serb.}$ (MeV/c) | $\Gamma^{Absorp.}$ (MeV/c) | $\sigma_{-n}$ (mb) | $\sigma_{E1}$ (mb) |
|---|---|---|---|---|---|---|---|
| $\{3/2^{+};0.00;0.73\}$ | $[0^{+} \otimes 0d_{\frac{3}{2}}]$ | 100 | 3.81 | 294 | 204.5 | 45.5 | 113.8 |
| $\{3/2^{+};0.55;0.73\}$ | $[2^{+} \otimes 1s_{\frac{1}{2}}]$ | 47 | 4.54 | 79 | 76.4 | 34.8 | 91.0 |
| $\{3/2^{+};0.55;0.73\}$ | $[0^{+} \otimes 0d_{\frac{3}{2}}]$ | 53 | 3.80 | 294 | 203.2 | 23.6 | 59.9 |
| $\{3/2^{+};0.55;0.73\}$ | 2 channels | 100 | 4.16 | 106 | 93.8 | 58.4 | 150.9 |
| $\{3/2^{+};0.20;0.73\}$ | $[2^{+} \otimes 1s_{\frac{1}{2}}]$ | 17 | 4.49 | 80 | 76.7 | 12.3 | 31.8 |
| $\{3/2^{+};0.20;0.73\}$ | $[0^{+} \otimes 0d_{\frac{3}{2}}]$ | 83 | 3.84 | 290 | 204.0 | 38.4 | 96.5 |
| $\{3/2^{+};0.20;0.73\}$ | 2 channels | 100 | 3.96 | 209 | 141.7 | 50.7 | 128.3 |
| $V_{so}$=0.5 MeV | | | | | | | |
| $\{3/2^{+};0.55;0.73\}$ | $[2^{+} \otimes 1s_{\frac{1}{2}}]$ | 67 | 4.58 | 79 | 76.1 | 50.6 | 132.4 |
| $\{3/2^{+};0.55;0.73\}$ | $[0^{+} \otimes 0d_{\frac{3}{2}}]$ | 33 | 3.70 | 300 | 205.1 | 13.8 | 34.4 |
| $\{3/2^{+};0.55;0.73\}$ | 2 channels | 100 | 4.31 | 89 | 83.0 | 64.4 | 166.8 |

Table 9

Results of calculations for the ground state of $^{17}$C with $J^{\pi}$=5/2$^{+}$. The calculated matter radius for the run $\{5/2^{+}; 0.00; 0.73\}$ is $R_m$=2.89 fm, while the run $\{5/2^{+}; 0.55; 0.73\}$ with all channels gives $R_m$=2.91 fm. The calculations are presented with usual spin-orbit force $V_{so}$=6.5 MeV (above) and small spin-orbit force $V_{so}$=0.5 MeV (below).

| Run | Channel | Weight | $R_{cn}$ | $\Gamma^{Serb.}$ | $\Gamma^{Absorp.}$ | $\sigma_{-n}$ | $\sigma_{E1}$ |
|---|---|---|---|---|---|---|---|
| $\{J^{\pi}; \beta; S_n\}$ | $[J_c \otimes j]$ | (%) | (fm) | (MeV/c) | (MeV/c) | (mb) | (mb) |
| $\{5/2^{+}; 0.00; 0.73\}$ | $[0^{+} \otimes 0d_{\frac{5}{2}}]$ | 100 | 3.93 | 284 | 203.4 | 49.5 | 124.5 |
| $\{5/2^{+}; 0.55; 0.73\}$ | $[2^{+} \otimes 1s_{\frac{1}{2}}]$ | 26 | 4.21 | 82 | 74.6 | 16.4 | 42.8 |
| $\{5/2^{+}; 0.55; 0.73\}$ | $[0^{+} \otimes 0d_{\frac{5}{2}}]$ | 74 | 4.24 | 265 | 198.3 | 44.5 | 117.0 |
| $\{5/2^{+}; 0.55; 0.73\}$ | 2 channels | 100 | 4.23 | 215 | 132.3 | 60.9 | 159.8 |
| $V_{so}$=0.5 MeV | | | | | | | |
| $\{5/2^{+}; 0.55; 0.73\}$ | $[2^{+} \otimes 1s_{\frac{1}{2}}]$ | 70 | 4.58 | 79 | 76.2 | 52.7 | 137.9 |
| $\{5/2^{+}; 0.55; 0.73\}$ | $[0^{+} \otimes 0d_{\frac{5}{2}}]^2$ | 30 | 3.58 | 313 | 207.1 | 11.6 | 28.4 |
| $\{5/2^{+}; 0.55; 0.73\}$ | 2 channels | 100 | 4.30 | 88 | 81.7 | 64.2 | 166.3 |

Table 10

Parameters used in the calculation for the $^{14}$C+n system.

| $S_n$ (MeV) | $E^{*}(2_1^{+})$ (MeV) | $R_o$ (fm) | $a$ (fm) | $V_{so}$ (MeV) | $\beta$ |
|---|---|---|---|---|---|
| 1.218 | 7.01 | 2.45 | 0.50 | 6.50 | 0.00 and 0.42 |

Table 11

Results of calculations for the ground state of $^{15}$C with $J^{\pi}$=1/2$^{+}$ and $S_n$=1.22 MeV [34]. The Γ=FWHM values in the case of absorption have been calculated according to equation (11) with parameters $R_t$=2.38 fm [28], $R_c$=2.45 fm and $R_n$=0.8 fm. The experimental $\Gamma^{Exp.}$, $\sigma_{-n}$ and $\sigma_{E1}$ values are 67±2 MeV/c, 33.5±0.7 mb and 75±2 mb [13] respectively. Calculated matter radius for the run $\{1/2^{+}; 0.00; 1.22\}$ is $R_m$=2.67 fm, while the run $\{1/2^{+}; 0.42; 1.22\}$ with all channels gives almost the same $R_m$=2.65 fm. The matter radius extracted from experiment is $R_m$=2.40±0.05 fm [28]. The EMD cross section is calculated on a $^{181}$Ta target at 83 MeV/u with parameters $R_t$=1.25·$A_t^{1/3}$ fm, $R_p$=2.45 fm.

| Run $\{J^{\pi}; \beta; S_n\}$ | Channel $[J_c \otimes j]$ | Weight (%) | $R_{cn}$ (fm) | $\Gamma^{Serb.}$ (MeV/c) | $\Gamma^{Absorp.}$ (MeV/c) | $\sigma_{-n}$ (mb) | $\sigma_{E1}$ (mb) |
|---|---|---|---|---|---|---|---|
| $\{1/2^{+}; 0.00; 1.22\}$ | $[0^{+} \otimes 1s_{\frac{1}{2}}]$ | 100 | 4.99 | 66 | 61.1 | 98.4 | 595.9 |
| $\{1/2^{+}; 0.42; 1.22\}$ | $[0^{+} \otimes 1s_{\frac{1}{2}}]$ | 88 | 5.01 | 66 | 60.8 | 87.1 | 531.5 |
| $\{1/2^{+}; 0.42; 1.22\}$ | $[2^{+} \otimes 0d_{\frac{3}{2}}]$ | 2 | 3.02 | 387 | 312.3 | 0.6 | 0.08 |
| $\{1/2^{+}; 0.42; 1.22\}$ | $[2^{+} \otimes 0d_{\frac{5}{2}}]$ | 10 | 2.94 | 395 | 314.3 | 3.5 | 0.4 |
| $\{1/2^{+}; 0.42; 1.22\}$ | 3 channels | 100 | 4.81 | 68 | 61.3 | 91.2 | 532.0 |

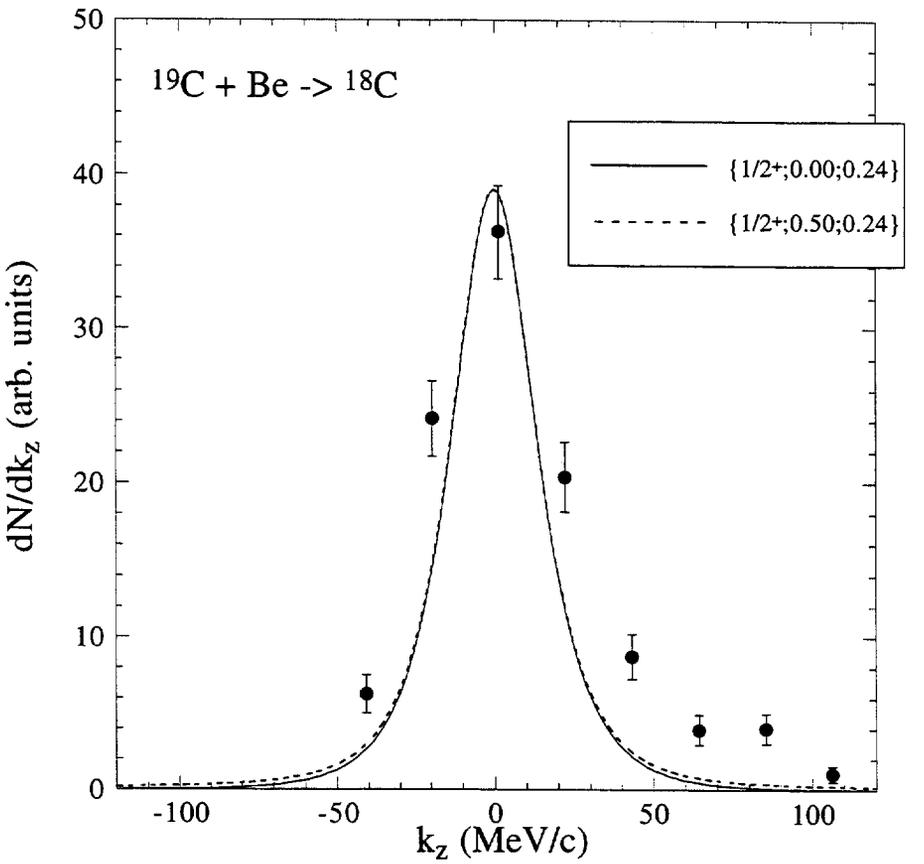


Figure 1: Longitudinal momentum distribution of $^{18}$C fragments from $^{19}$C ($J^{\pi}$=1/2$^{+}$) breakup reactions. The experimental data are taken at 77 MeV/u on a beryllium target [13].

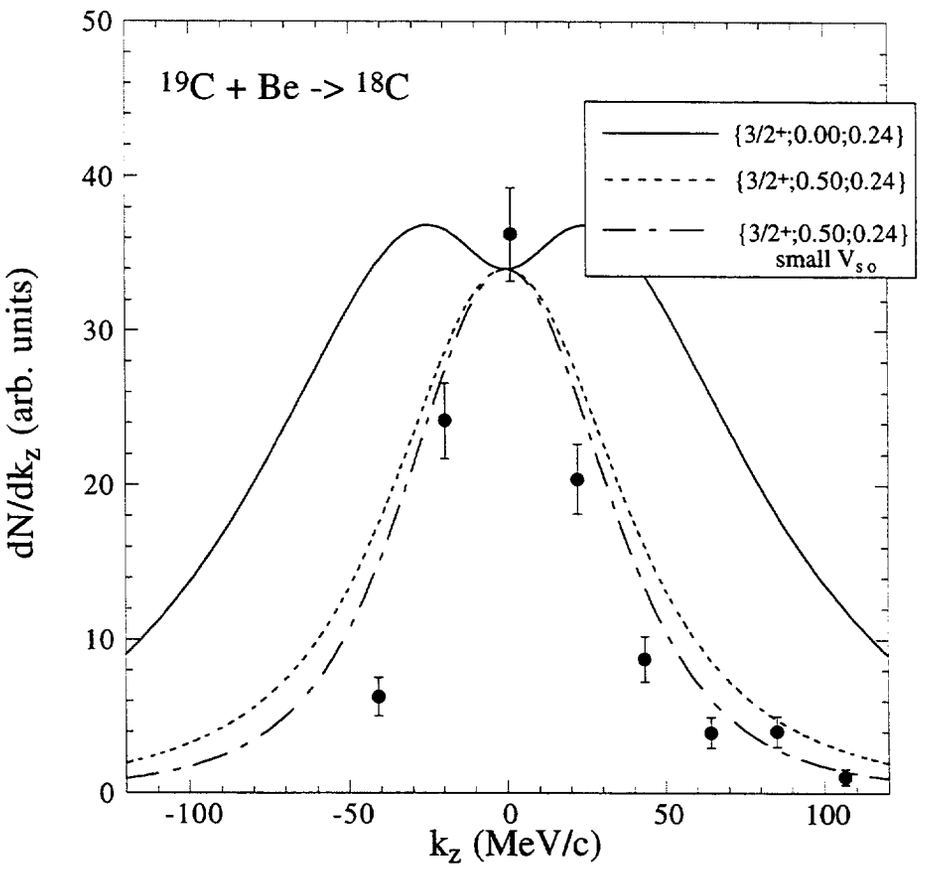


Figure 2: Longitudinal momentum distribution of $^{18}$C fragments from $^{19}$C ($J^{\pi}$=3/2$^{+}$) breakup reactions. The experimental data are taken at 77 MeV/u on a beryllium target [13].

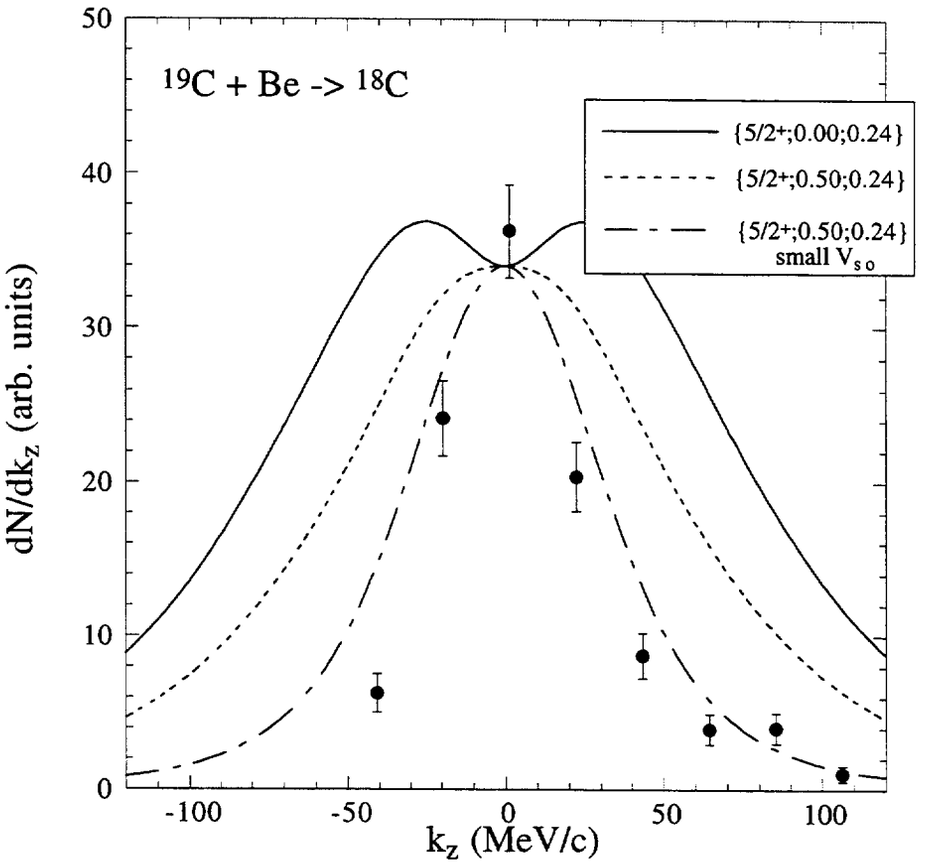


Figure 3: Longitudinal momentum distribution of $^{18}$C fragments from $^{19}$C ($J^{\pi}$=5/2$^{+}$) breakup reactions. The experimental data are taken at 77 MeV/u on a beryllium target [13].

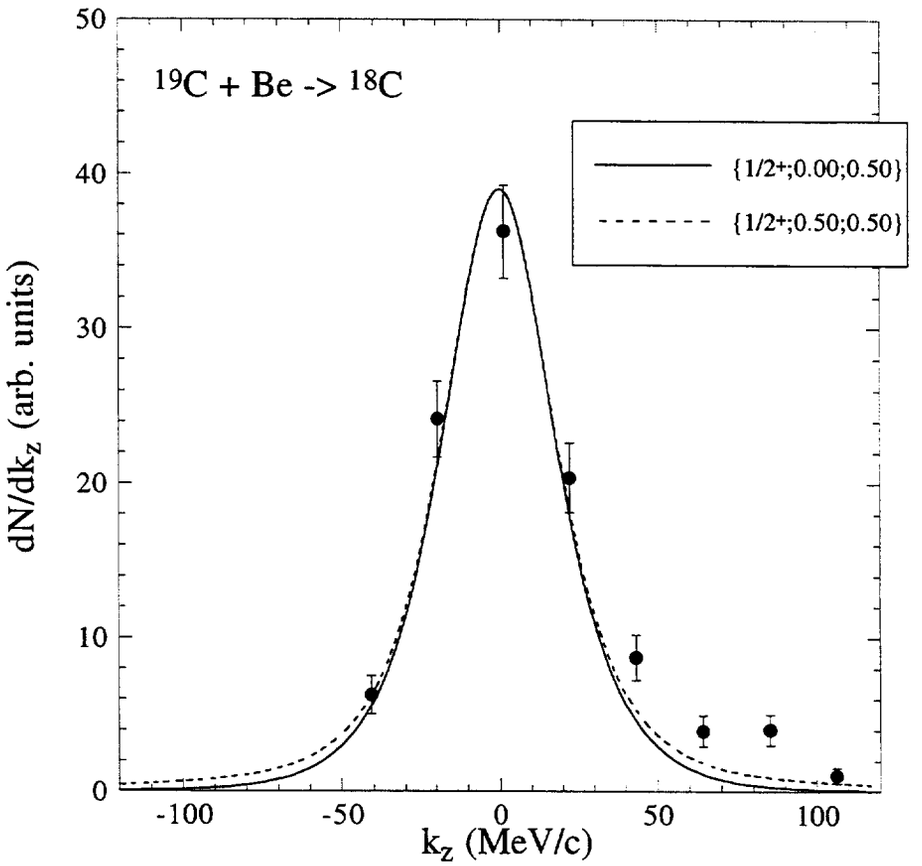


Figure 4: Longitudinal momentum distribution of $^{18}$C fragments from $^{19}$C ($J^{\pi}$=1/2$^{+}$, $S_n$=0.50 MeV) breakup reactions. The experimental data are taken at 77 MeV/u on a beryllium target [13].

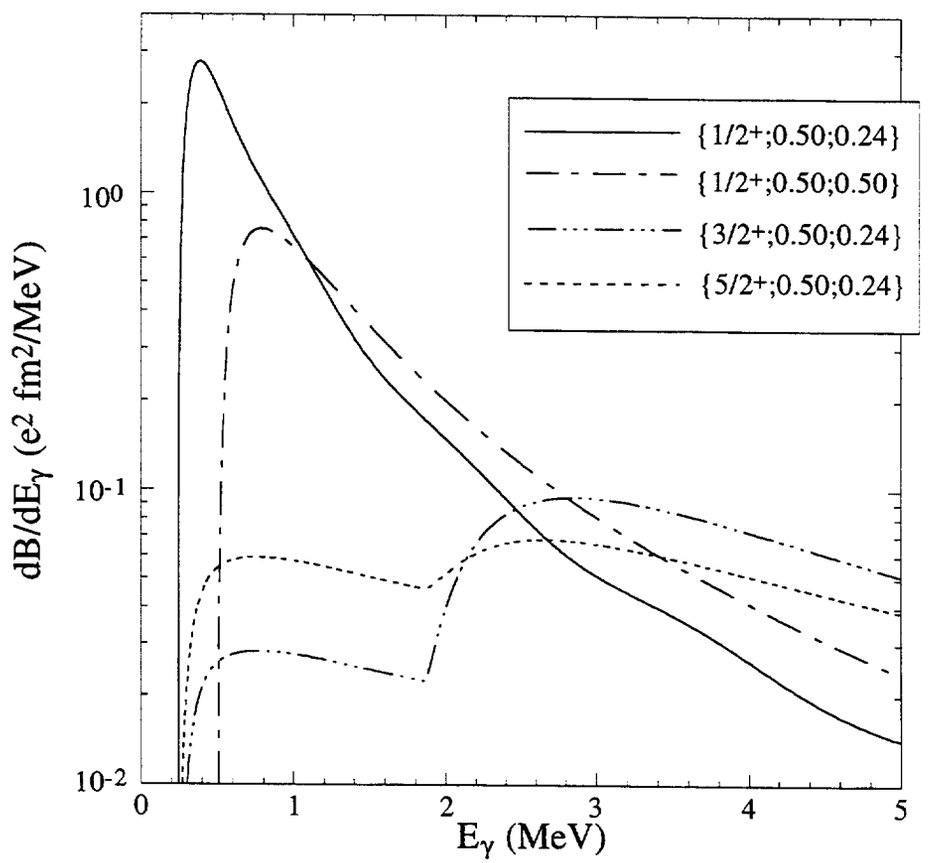


Figure 5: The $E1$ strength function for different $^{19}$C ground state configurations.

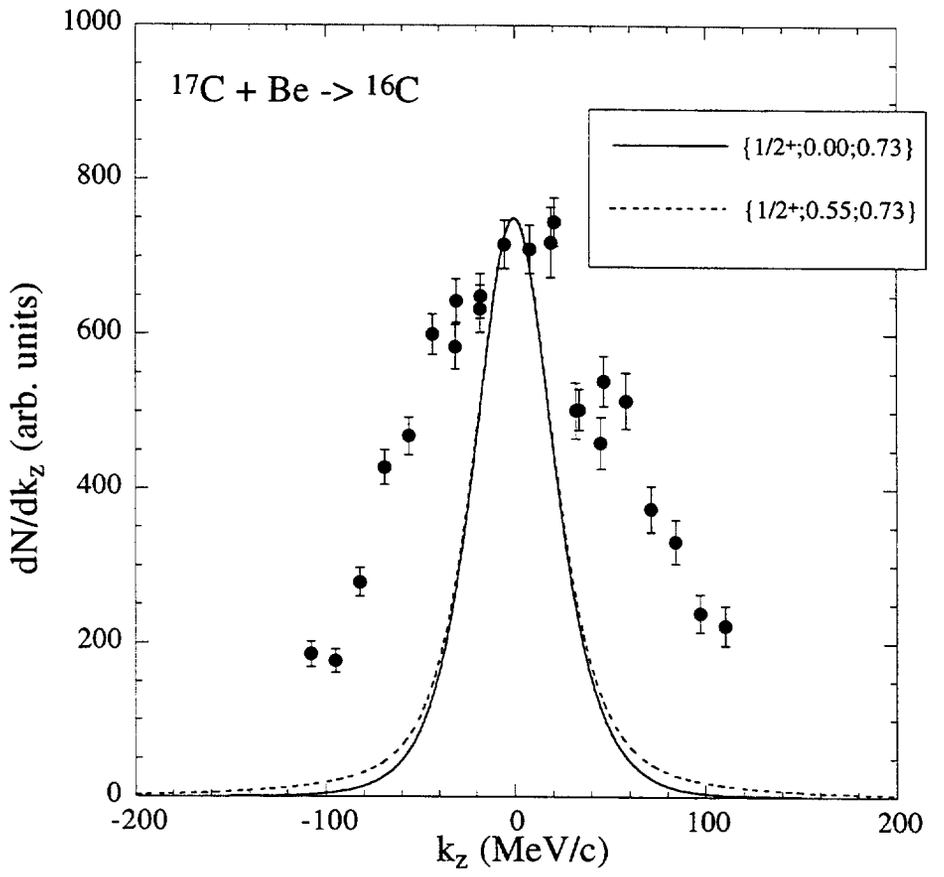


Figure 6: Longitudinal momentum distribution of $^{16}$C fragments from $^{17}$C ($J^{\pi}$=1/2$^{+}$) breakup reactions. The experimental data are taken at 83 MeV/u on a beryllium target [13].

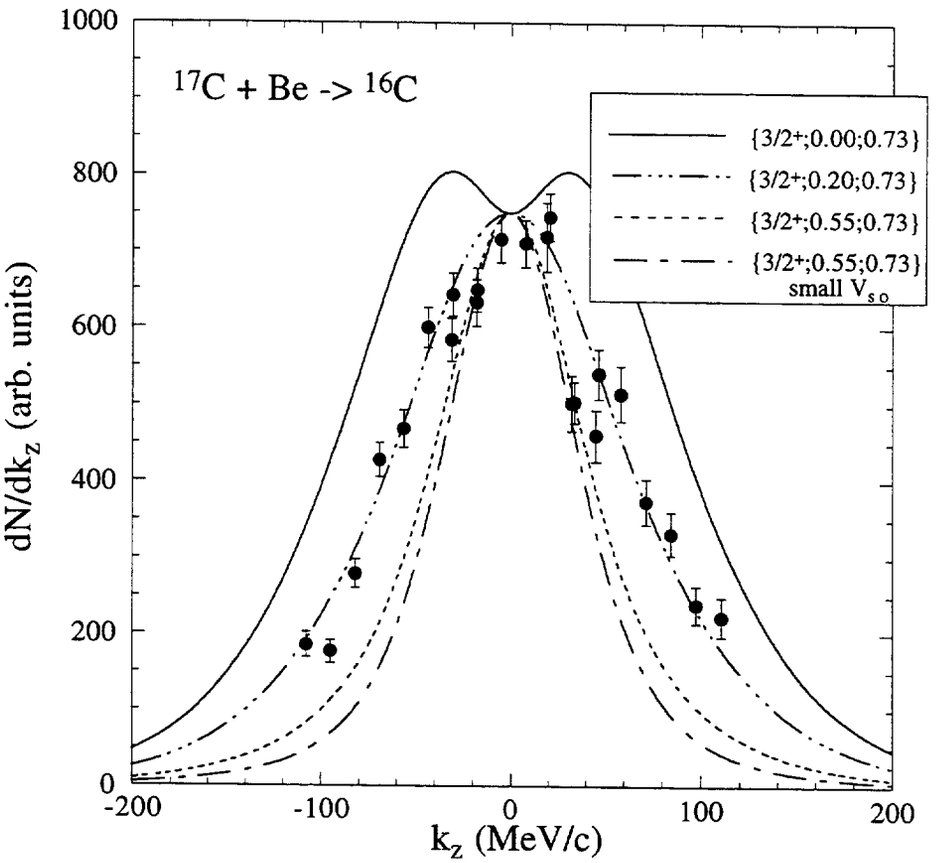


Figure 7: Longitudinal momentum distribution of $^{16}$C fragments from $^{17}$C ($J^{\pi}$=3/2$^{+}$) breakup reactions. The experimental data are taken at 83 MeV/u on a beryllium target [13].

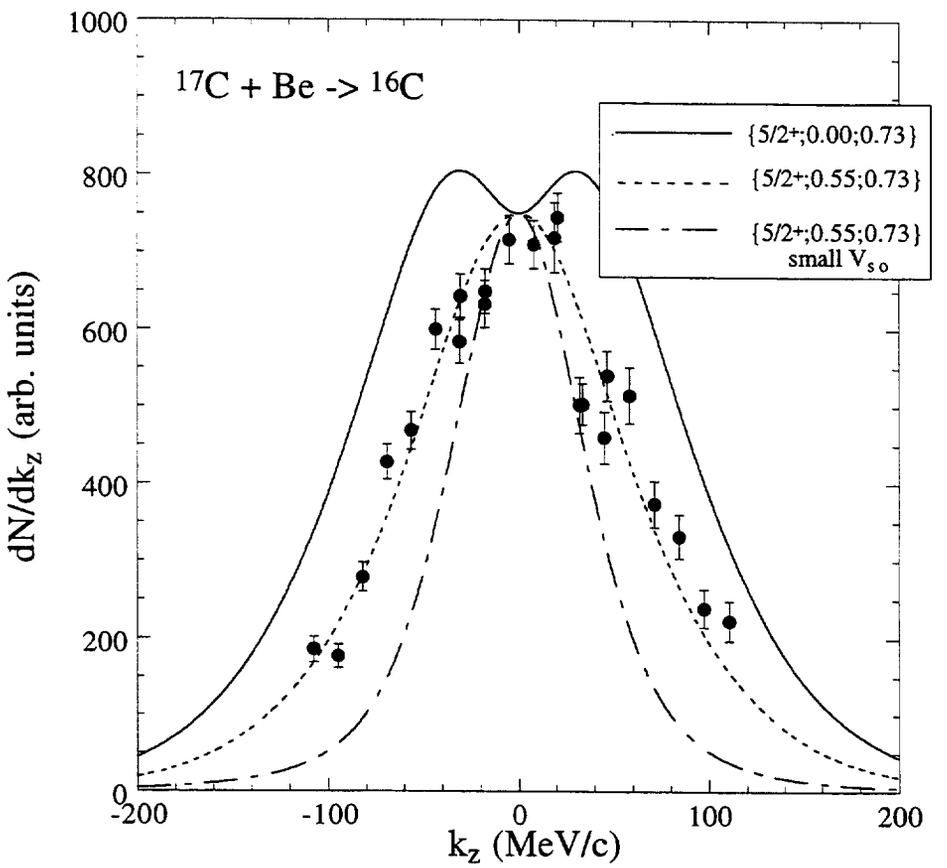


Figure 8: Longitudinal momentum distribution of $^{16}$C fragments from $^{17}$C ($J^{\pi}$=5/2$^{+}$) breakup reactions. The experimental data are taken at 83 MeV/u on a beryllium target [13].

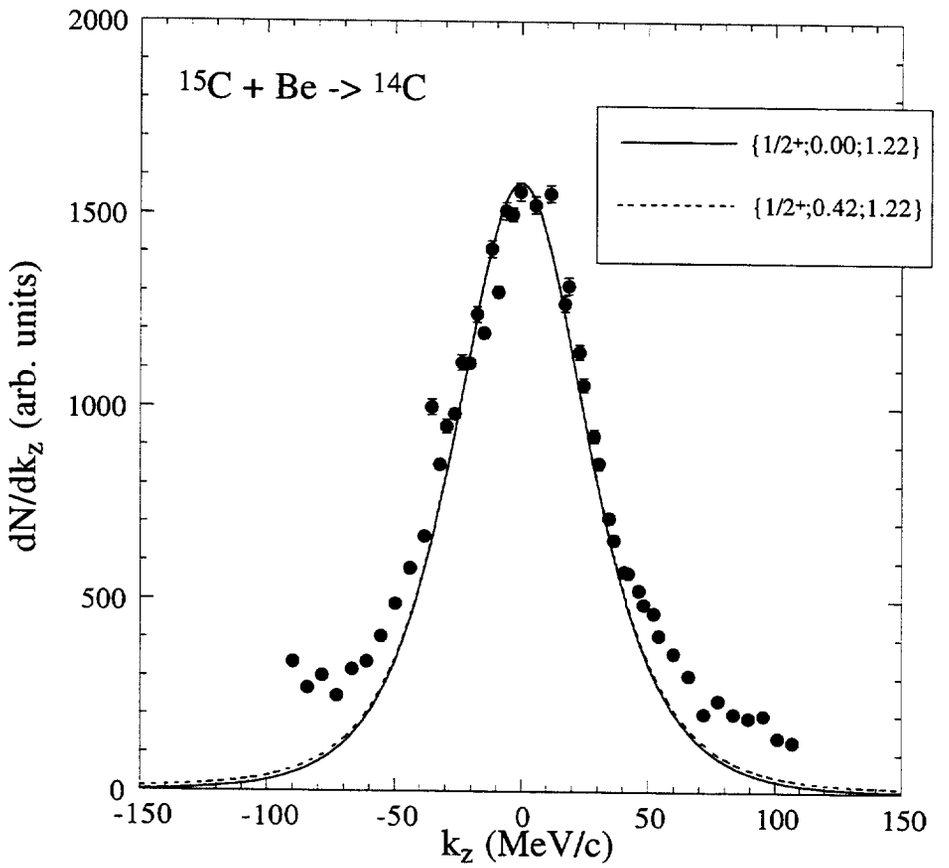


Figure 9: Longitudinal momentum distribution of $^{14}$C fragments from $^{15}$C ($J^{\pi}$=1/2$^{+}$) breakup reactions. The experimental data are taken at 83 MeV/u on a beryllium target [13].